ADVANCED FUNCTIONAL MATERIALS
www.afm-journal.de

Unraveling the Presence and Positions of Nitrogen Defects in Defective g-C_3N_4 for Improved Organic Photocatalytic Degradation: Insights from Experiments and Theoretical Calculations

*Yong Liu, Xiaochuan Chen, Mohammadreza Kamali, Barbara Rossi, Lise Appels, and Raf Dewil**

In this work, nitrogen-defective g-C_3N_4 with different nitrogen defect densities is synthesized for ciprofloxacin photocatalytic degradation. Compared with pristine g-C_3N_4, g-C_3N_4 etched with $NaBH_4$ for 1 h exhibits an approximately ten-fold increase in the rate constant of ciprofloxacin (CIP) degradation. The combined experimental analysis and theoretical calculations reveal that nitrogen defects can be incorporated into g-C_3N_4 in all nitrogen sites and that C—N═C is the most susceptible site. By incorporating nitrogen defects to induce defect states between the conduction band (CB) and valence band (VB), the electronic and band structures are tuned. The induced defect states can be downshifted to approach the valance band, reaching increased nitrogen defect density within optimum ranges to accommodate excited electrons to narrow the bandgap, extend the light absorption capability, and enhance the charge carrier separation and transfer efficiency. The g-C_3N_4 etched by $NaBH_4$ for 2 h with over-introduced nitrogen defects exhibits a declined performance due to a deteriorated structure, and the over-downshifted defect states turn out to be a new recombination center for charge carriers.

1. Introduction

Photocatalytic technologies, converting solar energy into chemical energy or electric energy, are one of the most sustainable strategies to alleviate the energy crisis and continuously worsening environmental issues.[1–3] Photocatalysis is a process where the semiconductor photocatalyst is activated by absorbing photons to generate excited electrons and holes, further initiating reduction or oxidation reactions depending on the conduction band (CB) and valence band (VB) edge position.[3,4] To date, various photocatalysts, including but not limited to titanium dioxide (TiO_2),[5] zinc oxide (ZnO),[6] cadmium sulfide (CdS),[7] vanadium oxide (V_2O_5),[8] zirconia (ZrO_2),[9] and graphitic carbon nitride (g-C_3N_4),[10] have been intensively developed and applied to environmental remediation. It is well known that the photocatalytic performance of these photocatalysts is highly dependent on the light absorption capacity (mainly determined by the energy band configuration), electron-hole pair separation efficiency, and consumption of the generated charge carrier.[4,11,12] Nevertheless, some metal or transition metal-based photocatalysts, such as TiO_2 and ZnO, with wide bandgaps can only absorb UV light, and some oxides, such as CdS, with a suitable bandgap to sensitize visible light may have heavy metal toxicity, hindering their practical applications.[1,3] As the field of study progressed, metal-free photocatalysts have drawn massive attention. g-C_3N_4, a metal-free visible-light photocatalyst with a narrow bandgap, has garnered significant attention in solar energy conversion, water splitting, and environmental remediation due to its easy synthesis, photostability, and chemical tunability.[13–15]

g-C_3N_4 composed of heptazine units is theoretically the more stable structure, and has a bandgap of 2.7 eV with CB and VB edge positions of −1.3 and 1.4 V (vs NHE), respectively.[16,17] Although g-C_3N_4 demonstrates many advantages, the practical implementation of pristine g-C_3N_4 is constrained by its restricted visible light absorption range, easy recombination of photogenerated electron-hole pairs, and low specific surface

Y. Liu, M. Kamali, B. Rossi, L. Appels, R. Dewil
Department of Chemical Engineering
Process and Environmental Technology Lab
KU Leuven
J. De Nayerlaan 5, Sint-Katelijne-Waver 2860, Belgium
E-mail: raf.dewil@kuleuven.be

X. Chen
College of Environmental and Resource Sciences and College of Carbon Neutral Modern Industry
Fujian Normal University
Fuzhou, Fujian 350000, China

B. Rossi, R. Dewil
Department of Engineering Science
University of Oxford
Parks Road, Oxford OX1 3PJ, UK

The ORCID identification number(s) for the author(s) of this article can be found under https://doi.org/10.1002/adfm.202405741

DOI: 10.1002/adfm.202405741

area.[17,18] Various strategies have been developed to improve the above deficiencies, such as elemental doping,[19,20] heterojunction construction,[21,22] surface modification,[23,24] and defect engineering,[18,25] to enhance the photocatalytic performance of g-C_3N_4. Among the different strategies, introducing nitrogen defects is effective in narrowing the bandgap, reducing the recombination of electron-hole pairs, and improving the specific surface area.[17] For instance, Tao et al. produced nitrogen-defective g-C_3N_4 by thermal polymerization of mixtures of urea and fumaric acid, which exhibited significantly improved photocatalytic hydrogen evolution, 2.64 times higher than that of pristine g-C_3N_4 due to the enhanced visible light absorption capacity, charge carrier separation efficiency and CB position downshifting.[18] In a study by Zhao et al., g-C_3N_4 with simultaneous boron doping and nitrogen defects, simply obtained via calcination of a mixture of g-C_3N_4 and $NaBH_4$ under a nitrogen atmosphere, showed markedly enhanced photocatalytic water oxidation performance attributed to the optimization of CB and VB positions for expanded light absorption range and creation of abundant unsaturated sites for promoted charge carrier transport.[26] Moreover, a fundamental understanding of the effect of nitrogen defects generated at different sites in g-C_3N_4 on photocatalytic activity has also been reported. For example, Li et al. revealed that the introduction of three coordinated nitrogen vacancies in g-C_3N_4 was responsible for the promoted visible light absorbance.[27] Wu et al. demonstrated that nitrogen vacancies generated in C-containing triazine ring sites introduced a defect state in the bandgap, boosting the light absorption capacity.[28] However, these studies focused on the single or separate effects of nitrogen defects, and the fundamental and mechanistic understanding of the synergistic effects of nitrogen defects generated at different sites remains unexplored. More notably, very few studies have been reported on nitrogen-defective g-C_3N_4-based photocatalysts for pollutant degradation in aqueous environments, which are more dependent on the driving force of excited electrons to form reactive species such as $\cdot OH$ and $\cdot O^{2-}$.[16] These previous reports suggest that with nitrogen defects incorporated into g-C_3N_4, improved performance in the photocatalytic degradation of pharmaceutical pollutants could be expected.

In this study, nitrogen-defective g-C_3N_4 was fabricated via simple $NaBH_4$ reduction with different treatment time. The obtained nitrogen-defective g-C_3N_4 was denoted as etched UCN-*x*h (x = 0, 0.5, 1, 2), where *x* represents the treatment time. The etched UCN-1 h exhibited the best photocatalytic performance for CIP degradation with the highest apparent kinetic constant of 0.046 min^{-1}, ≈10 times that of pristine UCN. The synergistic contribution of nitrogen defects generated in different sites to the promoted photocatalytic performance was explored from the viewpoint of the modulated electronic and band structures of g-C_3N_4. The experimental analysis and DFT calculations indicate that nitrogen defects could be introduced into UCN at all nitrogen sites, among which C-N═C is the most preferential site. The enhanced photocatalytic performance of etched UCN by incorporating nitrogen defects could be ascribed to the newly created discrete energy bands (defect states) between CB and VB, which result in both positive and negative effects according to the defect density on its photocatalytic performance. For the positive points, the defect states provide an extra path for excited electron transfer from VB maximum (VBM) to defect states except for the conventional routine from VBM to CB minimum (CBM) to enhance visible (e.g., solar) light harvesting and electron-hole pairs separation. The position of defect states is highly dependent on the defect density, which could move closer to VBM with increasing nitrogen defect density to accommodate more electrons excited by photons at longer wavelengths. With deeper downshifting to VBM in etched UCN-2 h, the defect state becomes a new center for the recombination of electrons and holes, leading to the deterioration of photocatalytic activity. Additionally, the evolution of the specific surface area and pore structures with longer treatment time also exhibits an important effect on the bandgap of etched UCN due to the quantum size effect.

2. Results and Discussion

2.1. Structure and Morphology

It has been reported that lattice N in g-C_3N_4 can be reduced into NH_3 by active hydrogen released from $NaBH_4$ during the treatment process.[26] There are three different types of N in g-C_3N_4, i.e., the N1 site of the N-C bridging structure connecting heptazine units, the N2 site of the C-N-C coordination structure in a heptazine unit, and the N3 site of the central N in a heptazine unit.[26] In principle, nitrogen defects could be produced in any of these N sites, which are expected to tune the band structure to alter the photocatalytic properties of UCN in our study. In addition, more nitrogen defects are expected to be incorporated into UCN with longer $NaBH_4$ treatment. The structures of the obtained UCN samples were studied by X-ray diffraction (XRD) patterns. In **Figure** 1a, two characteristic diffraction peaks at $2\theta = 12.7°$ and 27.5° are observed in pristine UCN, which are assigned to the in-plane structural packing of heptazine units (100) and the sheet interlayer stacking (002) of g-C_3N_4, respectively.[26] It is significant that the intensities and positions of these two peaks in etched UCN samples gradually decline and shift with the prolongation of $NaBH_4$ treatment time, indicating that $NaBH_4$ could react with UCN to introduce disorder into the structure of UCN.[26] Notably, the peak at $2\theta = 12.7°$ in etched UCN-2 h almost disappears, implying serious destruction of the in-plane structure in UCN.

Fourier transform infrared (FTIR) was further employed to disclose the molecular structures of the prepared UCN samples. In Figure 1b, the peaks at 810 cm^{-1} correspond to the bending modes of the heptazine units, while the peaks at 2900–3300 cm^{-1} originate from the N—H stretching vibrations.[26] In addition, the peaks located between 1750 and 1000 cm^{-1} are attributed to the stretching modes of aromatic C—N and C═N. Comparatively, with the prolongation of $NaBH_4$ treatment from 0 to 2 h, etched UCN displays a progressive decline in the intensity of C—N and C═N, and a new peak attributed to C≡N appears at ≈2180 cm^{-1} in the spectra.[29] These observations suggest that the $NaBH_4$ treatment introduced nitrogen defects into etched UCN and that the density of nitrogen defects increased with the prolongation of treatment time.

N_2 adsorption–desorption isotherms were applied to investigate the Brunauer–Emmett–Teller (BET) surface area and pore size distribution of UCN samples (Figure 1c), which indicate that all UCN samples display type IV curves with an H3 hysteresis loop, suggesting the presence of mesopores.[25,30] The specific

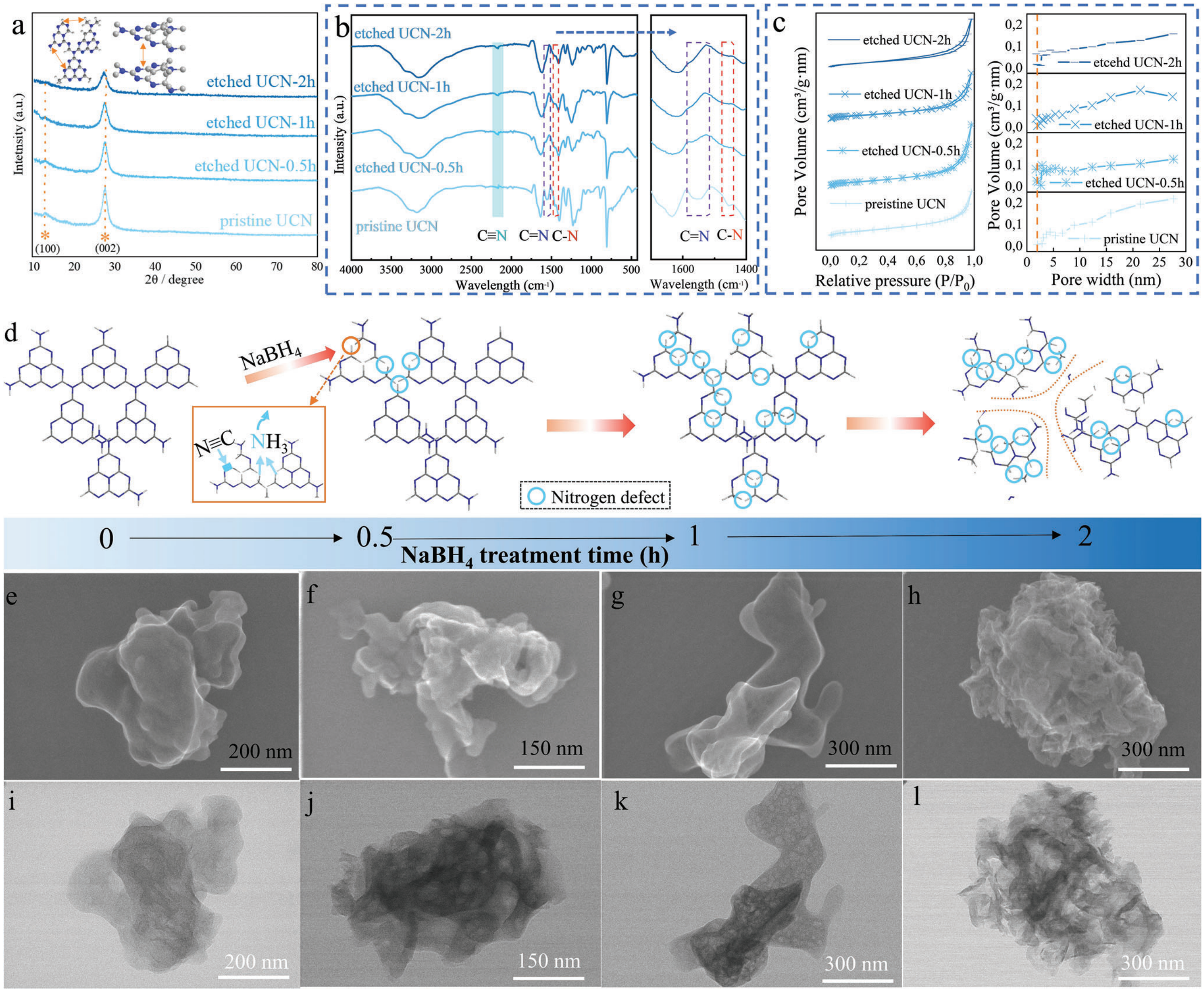

Figure 1. a) XRD patterns, b) FTIR spectra, c) N_2 adsorption–desorption isotherms and corresponding average pore size distribution curves, d) proposed structural changes in the heptazine units, e–h) SEM images, and i–l) TEM images of pristine UCN, etched UCN-0.5 h, etched UCN-1 h, and etched UCN-2 h.

surface area and pore parameters of the UCN samples are listed in Table S1 (Supporting Information). Pristine UCN exhibits a high pore volume with average pore diameters larger than 2 nm, which can be induced by CO_2 generation due to the existence of oxygen in urea during the synthesis process. The newly developed micropores in the etched UCN samples imply the generation of nitrogen defects by $NaBH_4$ treatment. Remarkably, the BET surface area decreased from 67.90 to 47.42 m^2 g^{-1} as the $NaBH_4$ treatment time increased from 0 to 1 h, which could be attributed to the agglomeration of the materials. The increase in pore volume from 0.1594 to 0.2117 cm^3 g^{-1} (from 0 to 0.5 h) and decrease from 0.2117 to 0.1618 cm^3 g^{-1} (from 0.5 to 1 h) could be explained by new pores developing through $NaBH_4$ treatment, while some enlarged pores may be congested due to accumulation, leading to a reduction in pore volume. With longer treatment time (from 1 to 2 h), the BET surface area increases from 47.42 to 53.36 m^2 g^{-1} along a slight increase of pore volume from 0.1618 to 0.1724 cm^3 g^{-1}, revealing that agglomerated etched UCN may be split into relatively smaller pieces and some pore structures may be destroyed as illustrated in Figure 1d.

The SEM images (Figure 1e–h) indicate that the UCN samples display an ultrathin nanosheet stacked structure, and the TEM images (Figure 1i–l) further reveal that new pores were introduced into etched UCN after $NaBH_4$ treatment and the number of pores increased with the prolongation of treatment time from 0 to 1 h. Notably, smaller deteriorated pieces of nanosheets could be observed in etched UCN-2 h, implying that excessive treatment time led to structure deterioration, as illustrated in Figure 1h,l.

2.2. Identification of Nitrogen Defects in Etched UCN

Room-temperature electron paramagnetic resonance (EPR) spectra were obtained to provide fingerprint evidence for proving the

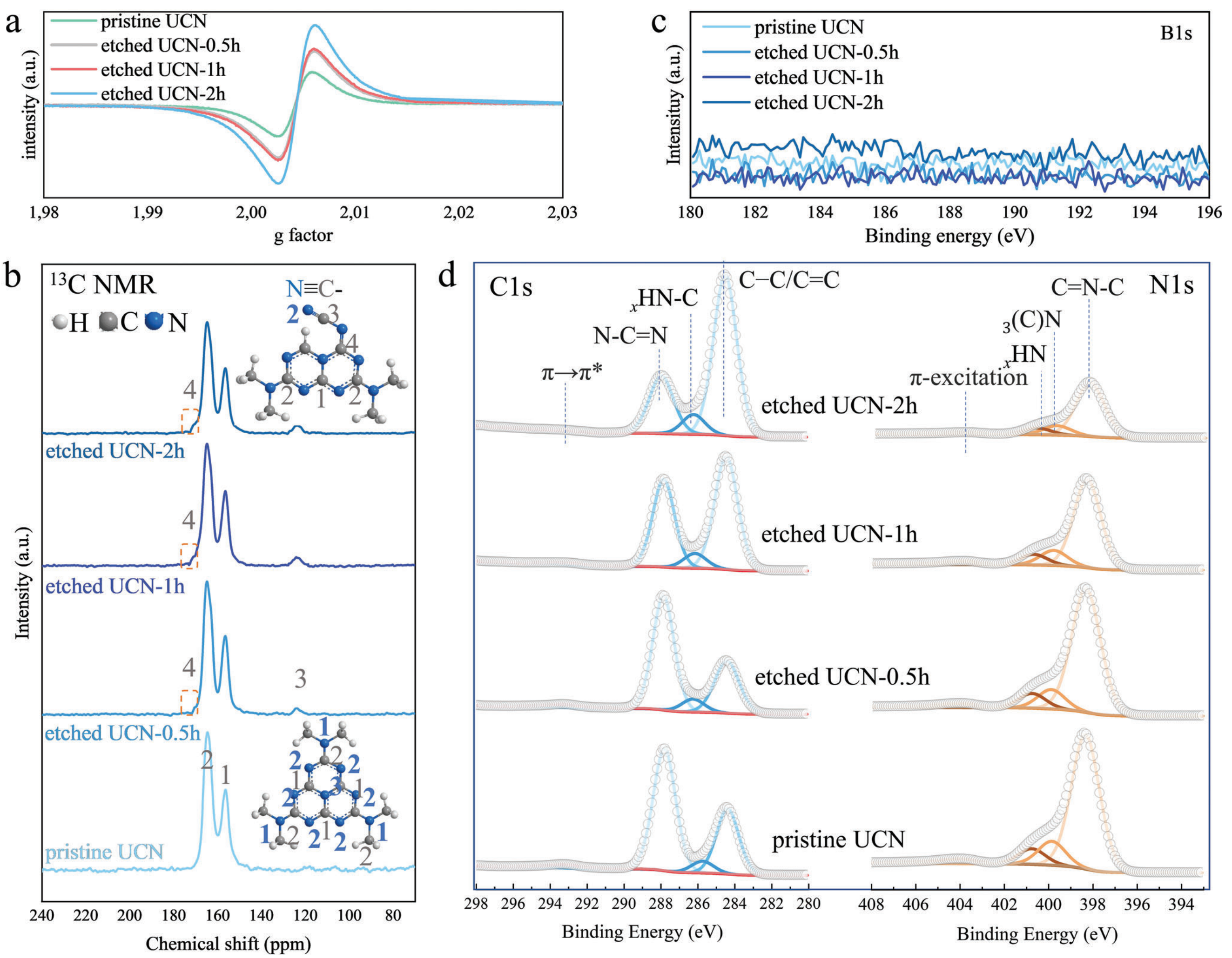

Figure 2. a) EPR spectra; solid-state magic angle spinning (MAS) ^{13}C NMR spectra, inset shows the proposed structure and NMR assignments for different carbon and nitrogen sites b); high-resolution B1s c), C1s, and N1s d) XPS spectra of all UCN samples.

existence of nitrogen defects in etched UCN. **Figure** 2a shows that all samples display a single Lorentzian line with a *g* value of 2.002 as the center of symmetry, which is assigned to the unpaired electrons in sp^2-carbon atoms within a heptazine-based g-C_3N_4.[25,26,30,31] The intensity of the Lorentzian line of etched UCN strengthened with the prolongation of $NaBH_4$ treatment from 0 to 2 h. The EPR intensity changes disclose the successful introduction of nitrogen defects into the etched UCN, which could open the heptazine units and thus donate a lone pair of electrons to the adjacent sp^2-carbon atoms.[25] Notably, the higher EPR intensity signal indicates a higher unpaired electron density, implying that prolonging $NaBH_4$ treatment time could enhance the density of introduced nitrogen defects.[26] Solid-state ^{13}C cross-polarization magic angle spinning nuclear magnetic resonance (CP-MAS-NMR) spectra were further recorded to identify the molecular structures of these samples, as shown in Figure 2b. Two strong peaks can be observed for all samples at 156.7 and 164.6 ppm attributed to the characteristic C1 atoms of $N2=C–N2(N3)$ and C2 atoms of $N2=C–N2(N1)$ in the heptazine units, respectively.[26,32] Notably, two new peaks appear at 123.6 and 171.5 ppm, which correspond to the characteristic C3 atoms of $C{\equiv}N2$ in the spectra of etched UCN samples and the C4 atoms neighboring C3, respectively.[26,33,34] The peak intensity of C3 was enhanced with the prolongation of $NaBH_4$ treatment time, indicating that longer treatment could increase the introduced nitrogen defect density, which is consistent with the EPR and FTIR results. Additionally, the reduced intensities of C3 and C4 also suggest that the introduced $C{\equiv}N2$ may arise from the decomposition of $N2=C–N2(N1)$ and $N2=C–N2(N3)$.[26,35]

Boron dopants and nitrogen defects were reported to be simultaneously incorporated at N sites of g-C_3N_4 by $NaBH_4$ thermal treatment, which remains controversial and needs further clarification due to the high dependence of successful boron dopants on treatment temperature and time.[26] Zhao et al. reported that boron dopants could be introduced into g-C_3N_4 by $NaBH_4$ thermal treatment for 12 h at temperatures higher than 350 °C.[26] Hence, X-ray photoelectron spectroscopy (XPS) was applied to analyze the surface chemical compositions of the prepared UCN samples. The survey XPS spectra (Figure S1, Supporting Information) demonstrate that all UCN samples display evident characteristic peaks of C, N, and O elements, where the peaks of O 1s are mainly assigned to the absorbed oxygen-containing species in the samples.[18,30] The increase in the XPS C/N ratio (Table S2, Supporting Information) on etched UCN samples with the prolongation of $NaBH_4$ treatment indicates the introduction of nitrogen defects. In contrast to pristine UCN, the content of nitrogen defects in etched UCN-0.5 h, etched UCN-1 h and etched UCN-2 h could be approximately estimated to increase by 2.80%, 27.2%, and 51.3%, respectively, according to the changes in the N ratio of the etched UCN samples (Table S2, Supporting Information) with the prolongation of the NaBH4 treatment. Importantly, no B1s signal (Figure 2c) is observed in any of the samples, revealing that little boron was doped by $NaBH_4$ treatment at 300 °C for 15 min in our experiment. In the C1s spectra (Figure 2d), the peaks located at 284.4, 286.6, 288.3, and 293.1 eV are assigned to adventitious C—C/C═C, C—NH/C—NH_2, N—C═N and π-electron delocalization in the conjugated systems. The significant increase in the peak intensity of C—C/C═C may be caused by the introduction of nitrogen defects. The intensity (peak area) of N—C═N in etched UCN samples weakens with the prolongation of $NaBH_4$ treatment, while that of N-H/N-H_2 increases gradually because the introduced C≡N shares a similar C1s binding energy with C-NH/C-NH_2,[36] implying the generation of nitrogen defects. The N1s spectra can be deconvoluted into four peaks at 398.4, 399.6, 400.8, and 403.2 eV, which correspond to C—N═C, N-$(C)_3$, N-H/N-H_2 and π excitation, respectively. The intensity of all N1s peaks is obviously weakened with the prolongation of $NaBH_4$ treatment, suggesting that the density of generated nitrogen defects increases accordingly and that nitrogen defects can be incorporated into all nitrogen sites. It has been reported that the preferential sites for the formation of nitrogen defects in g-C_3N_4 can be determined by comparing the atomic ratio discrepancy of different nitrogen groups based on the XPS results,[30,36,37] while this method is sometimes questionable and misleading because nitrogen defects could be introduced into any nitrogen sites in g-C_3N_4, leading to a decrease in the contents of all nitrogen groups. Therefore, it is more reasonable to predict the preferential nitrogen defect sites by calculating the relative area changes (compared to pristine UCN) of nitrogen groups in etched UCN samples based on XPS results (Table S3 and Figure S2, Supporting Information). The relative area of all nitrogen groups declines after $NaBH_4$ treatment, confirming that nitrogen defects could be introduced in all nitrogen sites. Importantly, C—N═C exhibits the most significant relative area change, implying that it is the preferential site for the incorporation of nitrogen defects. Additionally, the delocalization of π-electrons was considered to play a significant role in enhancing photogenerated charge carrier transfer.[38] The peak intensity of π-electron delocalization in C1s and N1s gradually decreases with the prolongation of $NaBH_4$ treatment (Figure 2d; Table S3, Supporting Information), which could lead to the decreased photocatalytic activity of etched UCN.

2.3. Band Structures

Compared to the pristine UCN, etched UCN samples with nitrogen defects exhibit significant changes in their optical properties, as depicted in **Figure 3a**, in which an obvious redshift in the absorption edge could be observed as the $NaBH_4$ treatment time increased from 0 to 1 h, while that of etched UCN-2 h blueshifts compared to etched UCN-1 h. Notably, wide extended absorption tails (Urbach tails) are also observed in the diffuse reflectance spectrometry (DRS) spectra and demonstrate similar change trends as absorption edge shifting in all UCN samples, implying that new nitrogen defect-related intermediate states are introduced to tune the band structure of UCN,[25,26] with the bandgap narrowing from 2.71 eV for pristine UCN to 2.59 eV for etched UCN-1 h (Figure 3b). The VB XPS spectra (Figure 3c) demonstrate that the VBM position decreases from 1.71 eV for pristine UCN to lower energies for etched UCN depending on the $NaBH_4$ treatment time.

Structural lattice disorder and crystal defects could introduce tail-like energy levels between the CB and VB to form defect states, which are known as Urbach tails.[25] Urbach energy, representing the energy gap between these Urbach tails, is used to decipher the effects of the Urbach tail on the bandgap tuning of semiconductor materials, which can be calculated by Equation (1).[25,39,40]

$$\alpha = \alpha_0 \exp\left(h\nu/E_u\right) \tag{1}$$

where α is the absorption coefficient, α_0 is a constant, $h\nu$ is the photon energy and E_u represents the Urbach energy. E_u could be determined by calculating the reverse slope of the linearly fitted line of lnα versus E_u. A higher E_u indicates higher structural disorder or more defects. Figure 3d shows that the E_u of etched UCN gradually increases from 1.255 to 1.392 with the prolongation of $NaBH_4$ treatment time from 0 to 2 h, suggesting that more nitrogen defects were incorporated with longer treatment. Combining the changes in the bandgap with E_u by different $NaBH_4$ treatment time reveals that the positions of the Urbach tails (defect states) could be shifted closer to the VBM with increasing nitrogen defect density in etched UCN. The effects of defect states introducing and shifting by regulating the introduced nitrogen defect density will be discussed detailly in Section 2.5.1 with DFT calculations. Notably, the quantum size effect arises when the size of a material becomes small enough that its electronic properties are changed, which leads to different properties from its bulk counterpart.[41] The photon energy difference (ΔE_u) between etched UCN-0.5 h and etched UCN-1 h is larger than that between etched UCN-1 h and etched UCN-2 h, as shown in Figure 3e, implying that some defects in etched UCN-2 h further deteriorated, leading to a reduction in particle size and structure disorder. Combined with the calculated bandgap values, the band positions of the UCN samples are shown in Figure 3f, where both the positions of CB and VB are continuously tuned with different introduced nitrogen defect densities. Hence, the slightly increased bandgap of etched UCN-2 h compared to etched UCN-1 h may be attributed to the quantum size effect induced by the smaller size of etched UCN-2 h nanosheets, as suggested by the TEM and BET results, where the photogenerated electrons and holes are confined by the potential barrier in the materials, leading to the enhancement of the bandgap.

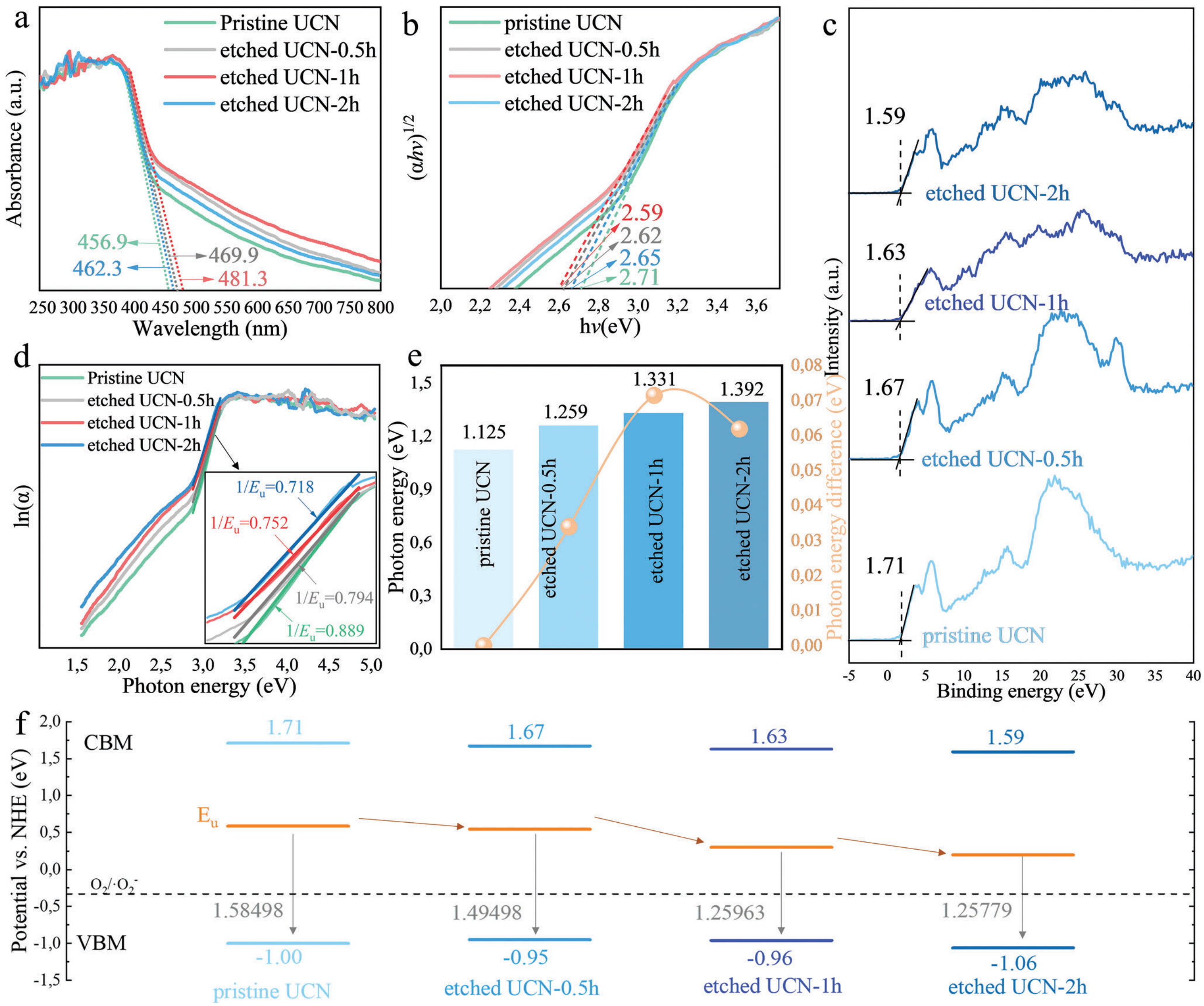

Figure 3. a) UV–vis DRS, b) plots of transformed Kubelka-Munk function versus photon energy, c) VB XPS spectra, d) Urbach energy, e) the respective photon energy difference and f) band structure alignments of UCN samples.

2.4. Photocatalytic Performance for CIP Degradation of UCN Samples

To understand the effects of the position and amount of generated nitrogen defects on the photocatalytic performance of nitrogen-defective UCN, the degradation of CIP by different UCN samples under simulated solar light irradiation was performed. It is well known that the adsorption of pollutants by photocatalysts is the first step for efficient photocatalytic degradation.[3] Hence, the adsorption of CIP by pristine and etched UCN was investigated, as shown in Figure S3 (Supporting Information). In contrast, pristine UCN exhibited the lowest adsorption capacity for CIP with a removal efficiency of 3.8% at equilibrium. $NaBH_4$ treatment enhanced the adsorption capacity of etched UCN for CIP, and the adsorption capacity increased with increasing treatment time, where etched UCN-0.5 h, UCN-1 h, and etched UCN-2 h demonstrated removal efficiencies of 13.9%, 20.6% and 23.1%, respectively, at equilibrium. The improved adsorption capacity could be ascribed to the modified pore structure in the etched UCN as revealed by the BET and TEM results, where new pores could be introduced by $NaBH_4$ treatment to provide more active sites for adsorption.

The performance of various UCN samples on photocatalytic degradation of CIP was further studied. **Figure** 4a–c shows that the CIP photocatalytic degradation efficiencies by etched UCN were obviously better than that by pristine UCN, where the etched UCN-1 h exhibited the best photocatalytic performance with 98.8% CIP degradation efficiency ($k_{app} = 0.0461$ min^{-1}), while only 42.3% of CIP was removed ($k_{app} = 0.00479$ min^{-1}) by pristine UCN under the same experimental conditions. The etched UCN-2 h had the worst performance with 88.8% CIP degradation efficiency ($k_{app} = 0.0129$ min^{-1}) compared to the other etched UCN, implying that overgenerated nitrogen defects may destroy the structure of etched UCN to abate its

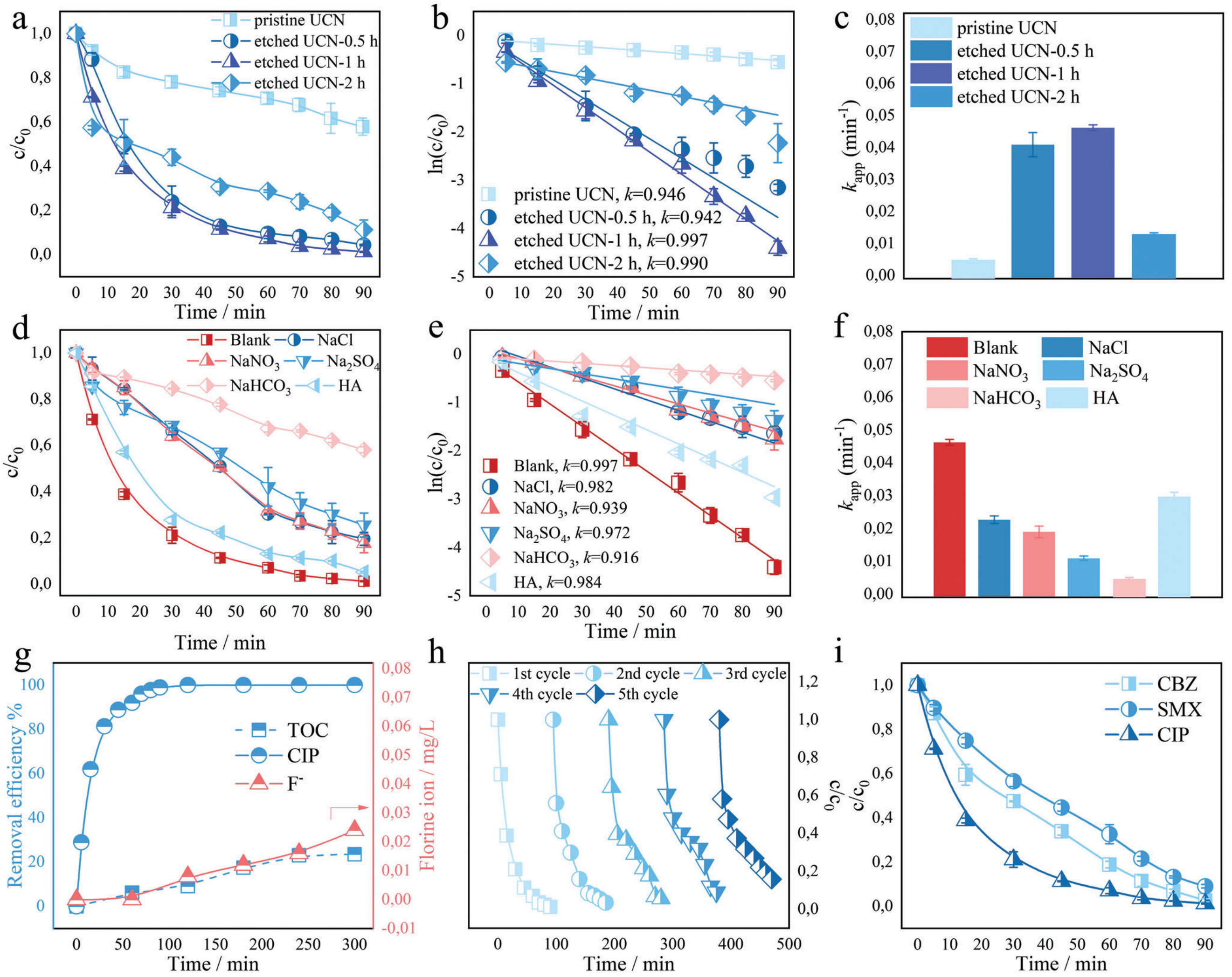

Figure 4. Photocatalytic degradation of CIP by a) UCN samples, b) kinetics and c) degradation rates, conditions: $[\mathrm{CIP}]_0 = 2.5$ mg L^{-1} (200 mL with $[\mathrm{F}]_0 = 0.1435$ mg L^{-1}), initial pH ≈ 6.0, [pristine/etched UCN] = 0.5 g L^{-1}, and simulated sunlight; Effects of chloride (5 mM), nitrate (5 mM), sulfate (5 mM), and bicarbonate (5 mM), and HA (10 mg L^{-1}) on the photocatalytic degradation of CIP by d) etched UCN-1 h, e) kinetics, and f) degradation rates; TOC removal and defluorination efficiency by etched UCN-1 h g); evaluation of reusability of etched UCN-1 h for CIP photocatalytic degradation h); photocatalytic degradation of CIP, CBZ, and SMX by i) etched UCN-1 h, conditions: $[\mathrm{CIP}]_0 = [\mathrm{CBZ}]_0 = [\mathrm{SMX}]_0 = 2.5$ mg L^{-1}.

photocatalytic properties. Therefore, DFT calculations will be further carried out in Section 2.5.1 to evaluate the effect of the amounts and positions of generated nitrogen defects in etched UCN on the band structure tuning and separation efficiency of photogenerated charge carriers. A comparison of g-C_3N_4-based photocatalysts for photocatalytic degradation of CIP in the current and previous studies is demonstrated in Table S4 (Supporting Information). Comparatively, etched UCN-1 h exhibited excellent photocatalytic performance toward CIP degradation with a higher reaction rate, indicating its promising potential for practical wastewater treatment.

2.4.1. *Influences of Water Matrix*

The water matrix exhibits an important effect on the application of photocatalysis-based AOPs for wastewater treatment.[42–44] Hence, the impact of common naturally organic components (humic acid, HA) and inorganic substances (i.e., chloride, nitrate, sulfate, and bicarbonate) in wastewater on the photocatalytic degradation of CIP by etched UCN-1 h was investigated, as depicted in Figure 4d–f. The results demonstrate that the presence of these typically present substances in aquatic environments exerted detrimental effects on CIP degradation by etched UCN-1 h to a certain extent. Comparatively, bicarbonate demonstrated the most significant inhibitory effect on CIP degradation, where k_{app} decreased from 0.0461 to 0.0046 min^{-1} after introducing bicarbonate into the system. Bicarbonate is commonly recognized as a •OH scavenger in AOPs according to Equation (2), where $CO_3^{\bullet-}$ with higher selectivity toward attacking electron-rich compounds such as phenols, S and N-containing compounds could be produced.[45] The generated $CO_3^{\bullet-}$ may have a lower selectivity toward CIP due to the strong electron withdrawing ability of C-F in CIP, leading to the decline of CIP degradation in our system.[44,46] In addition, the introduction of bicarbonate could also alter the solution pH, as shown in Figure S4 (Supporting Information), where the pH increased from 5.50 to 8.85. CIP exists as different dissociations at different pH levels, where CIP mainly consists of CIP^+ and CIP^{+-} at pH 5.5 and 8.85, respectively. Notably, CIP^{+-} is reported to be more reactive than CIP^+ in our previous study.[47] Therefore, the inhibited CIP degradation by introducing bicarbonate could be ascribed to its effects on radical scavenging and CIP species tuning by changing the solution pH. In the case of adding chloride, nitrate and sulfate, the pH of the systems was slightly increased from ≈5.5 to 5.7–5.8, and similar negative effects on CIP degradation were observed with rate constants of 0.023, 0.019, and 0.011 min^{-1}, respectively. Hence, the negative effects of chloride and sulfate may mainly arise from the sacrifice of •OH (oxidation potential 2.80 V) to form less active radicals such as $\bullet Cl_2^-$ (oxidation potential 1.36 V) and $\bullet SO_4^-$ (oxidation potential 2.60 V) by consumption.[48] Noticeably, nitrate is regarded as a potential source of ·OH formation (Equations (3) and (4)) to promote the degradation of organic pollutants in photochemical AOPs with UV irradiation (200–420 nm).[42] Nevertheless, nitrite may also be produced in photochemical AOPs at a wavelength of 254 nm in Equation (5), which could further inhibit the performance of the corresponding process by rapidly reacting with radicals.[42] In our case, the negative effect of produced nitrite may be more significant than that of extra formed •OH by adding nitrate into the system, leading to a decrease in CIP degradation. Additionally, the introduction of HA had the slightest effect on CIP degradation, where 94.9% CIP degradation efficiency was achieved in 90 min. Although the presence of these natural components has certain negative effects on CIP degradation by etched UCN-1 h, 80.5%, 82.5%, 74.5%, 42.0%, and 94.9% CIP degradation efficiency could be obtained with 5 mᴍ chloride, nitrate, sulfate, and bicarbonate and 10 mg L^{-1} HA, respectively, within 90 min, implying the promising potential of nitrogen-defect UCN for practical wastewater treatment.

$$\bullet OH + HCO_3^- \rightarrow CO_3^{\bullet -} + H_2O \tag{2}$$

$$NO_3^- + h\nu \rightarrow \bullet NO_2 + \bullet O^- \tag{3}$$

$$\bullet O^- + H_2O \rightarrow \bullet OH + OH^- \tag{4}$$

$$NO_3^- + h\nu \rightarrow NO_2^- + O\left(^3P\right) \tag{5}$$

2.4.2. Mineralization and Detection of Inorganic Ions

The removal of total organic carbon (TOC) and release of F^- were measured to evaluate the mineralization of CIP during the photocatalytic degradation process by etched UCN-1 h. Figure 4g shows that CIP was completely degraded within 120 min, while the highest TOC removal efficiency was only 23.5% after 300 min of treatment. In addition, F^- arising from CIP defluorination gradually accumulated in the system, while only 0.024 mg L^{-1} of F^- (the theoretical F concentration of 10 mg L^{-1} CIP solution is 0.574 mg L^{-1}) was detected within 300 min. The complete CIP degradation, low TOC removal, and slight defluorination efficiency suggest that CIP may be more susceptible to reactive species attack, while the generated small degradation intermediates are more resistant to further mineralization, as reported by other studies.[49,50]

2.4.3. Stability and Versatility of Etched UCN

The stability and reusability of the prepared etched UCN-1 h was first evaluated by 5 consecutive cycles for CIP degradation, as presented in Figure 4h. The result demonstrates that the CIP degradation by etched UCN-1 h could still maintain 98% within 90 min after the 5th cyclic process, implying the good stability and reusability of etched UCN-1 h. Furthermore, the etched UCN-1 h after the 5th reaction cycle was characterized by XRD, FTIR and STEM. The XRD and FTIR results in Figures S5 and S6 (Supporting Information) revealed that there was no significant change observed between the fresh and used etched UCN-1 h, indicating the stability of etched UCN-1 h. From Figure S7 (Supporting Information), the morphology of the etched UCN-1 h still maintained the same ultrathin structure as the fresh sample, further confirming its good stability. In addition, real wastewater may contain various organic contaminants, so the versatility of etched UCN-1 h was further evaluated by testing its photocatalytic performance for the degradation of the other common pharmaceutical pollutants, i.e., carbamazepine (CBZ) and sulfamethoxazole (SMX) as shown in Figure 4i. Etched UCN-1 h also exhibited good performance in the degradation of CBZ and SMX, where 97.4% and 91.0% degradation efficiency, respectively, was achieved in 90 min under the same experimental conditions as CIP. The above results indicate that etched UCN-1 h is a promising photocatalyst for practical application in the field of wastewater treatment with organic pollutants.

2.5. Mechanism for the Improved Photocatalytic Activity of Etched UCN

2.5.1. Modified Electronic Structure

The DRS results also verify that the band structure of etched UCN was tuned continuously with the prolongation of $NaBH_4$ treatment time. The experimental results demonstrated that etched UCN-1 h exhibited the best performance for CIP photocatalytic degradation compared to etched UCN-0.5 h and etched UCN-2 h, implying that the amount and generated position of N vacancies may have critical influences on the photocatalytic effect. Therefore, theoretical calculations were further carried out to evaluate the effect of the amounts and positions of generated N vacancies on the electronic band structure and separation efficiency between photogenerated electrons and holes. Figure S8a (Supporting Information) displays the optimized geometric structure of the pristine heptazine-based $g\text{-}C_3N_4$. As we mentioned above, there are three possible types of N (i.e., N1, N2 and N3) in $g\text{-}C_3N_4$ for the formation of N vacancies. The theoretical formation energies (E_f) of N vacancies in these different sites were first qualitatively analyzed to address the formation difficulty (Figure S8b, Supporting Information). The computational results show that N2 is most active with the lowest E_f of 1.858 eV, while N1 is most stable with the highest E_f of 6.682 eV, suggesting that N2 is the

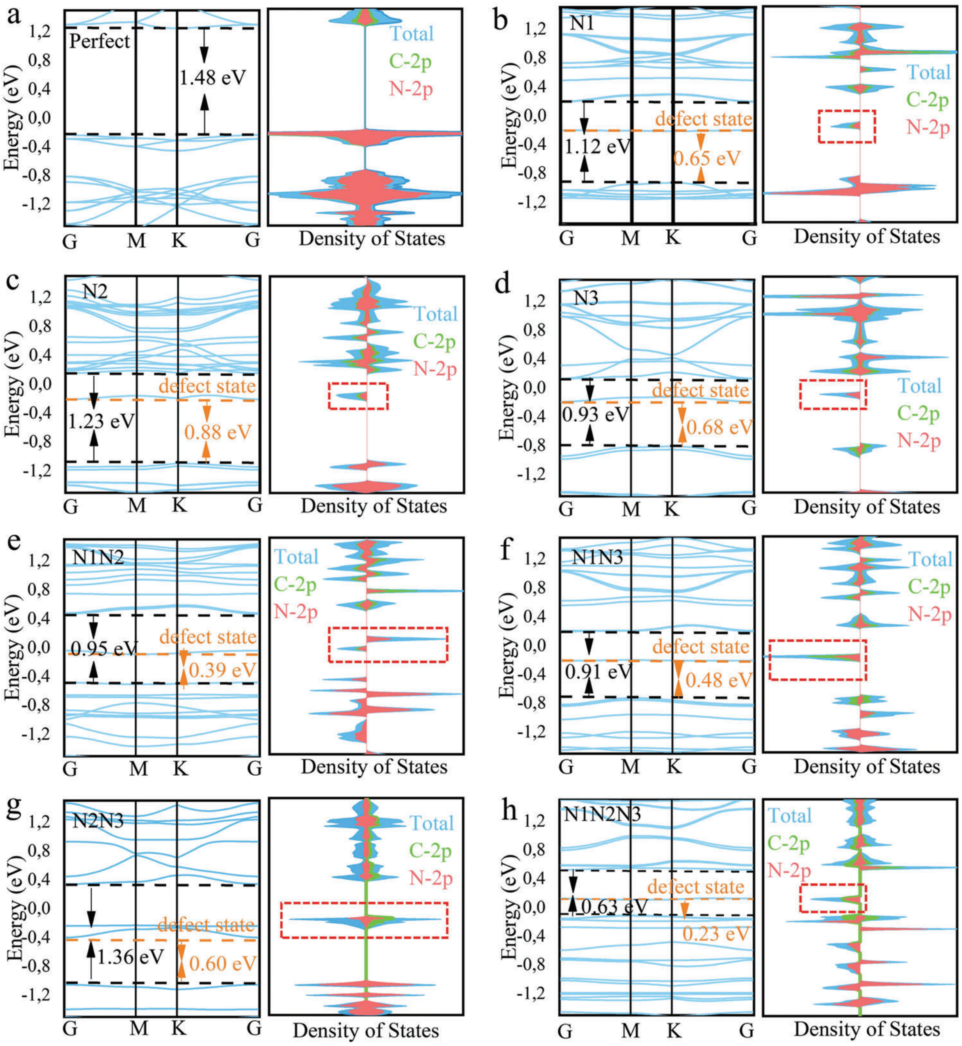

Figure 5. Calculated spin-polarized band structures and the corresponding PDOS of perfect g-C_3N_4 a) and N-defective g-C_3N_4 with b) N1, c) N2, d) N3, e) N1N2, f) N1N3, g) N2N3 and h) N1N2N3 defect sites.

preferential site for the formation of N vacancies. The obtained preference for the formation of N vacancies is consistent with a previous report,[25,30] and is also in good agreement with the XPS results in Section 2.2, where C═N-C is the most susceptible site for the incorporation of nitrogen defects. It is worth noting that it is possible to generate N vacancies in N1 and N3 in etched UCN despite the higher E_f values, especially prolonging the treatment by $NaBH_4$.

The impact of introducing N vacancies in g-C_3N_4 on the evolution of the electronic structure was further evaluated, where we compare the structures with single N defect at three different sites (N1, N2, N3), double N defects at two different sites (N1N2, N1N3, N2N3) and triple N defects at all sites (N1N2N3), as shown in Figure S8c–i (Supporting Information). The bandgap of g-C_3N_4 calculated by the GGA-PBE functional is smaller than the experimental values because of the well-known limitation of DFT.[25,51,52] As mentioned, we mainly focus on the evaluation of the effect of N vacancies on the electronic structures of g-C_3N_4, which is expected to be achieved accurately enough by GGA-PBE, as reported previously.[25,53,54] In **Figure 5**a, the theoretically calculated electronic structure discloses that pristine g-C_3N_4 has an indirect bandgap of 1.48 eV with the CBM and VBM located at the K point and G point, respectively. According to the calculated electronic structures, some significant changes could be observed after incorporating nitrogen defects in g-C_3N_4, where nitrogen defects 1) narrow the bandgap (the bandgap decreases with increasing nitrogen defect density generally) and 2) lead to a shifting of CB and VB, implying that the electronic structure of g-C_3N_4 is tuned by introducing nitrogen defects, as reported.[11] The calculated bandgap of the structure with N1N2N3 defects is most significantly reduced to 0.63 eV in Figure 5h. The narrowed bandgap and shifting of the CB and VB are in good agreement with the extended optical absorption observed in the DRS data. There is no significant difference among the bandgap values when a single N defect is introduced. However, a significant difference is observed when double N defects are incorporated, where the bandgap of the structure with N2N3 defects (Figure 5g) exhibits a much greater value of 1.36 eV than that with N1N2 and N1N3. This could be explained by the structural changes and charge carrier redistribution arising from the introduction of N vacancies at different sites.[55] Figure S8a (Supporting Information) shows that the bridge atom N1 connecting three heptazine units plays a more important role in maintaining structural stability than does edge N2 and inner N3.[18,53] In addition, the calculation results also demonstrate that N1 is the most stable N site, with the highest E_f of 6.682 eV. Hence, it could be inferred that more significant structural collapse occurs when N1 is removed than when N2 or N3 is removed.[56] It is worth mentioning that introducing a single N defect may hardly lead to significant structural collapse, which could explain why there is no significant bandgap difference between structures with a single N defect at different N sites. The impact of N defects, especially N1 defects, could be amplified by increasing the number of introduced defects.[55] The structure with N2N3 defects is more stable than that with N1N2 and N1N3 defects because N1 still connects the destroyed heptazine unit with two perfect heptazine units in its structure. The destroyed heptazine unit in the structures with N1N2 and N1N3 defects is disconnected from the other heptazine units, leading to more significant structural collapse. Therefore, the structural collapse induced by incorporating different N defects is beneficial for modifying the electronic structure of g-C_3N_4, which will be further investigated by partial density of states and molecular orbital analysis. Additionally, it should be noted that the impact of N1 may be magnified by these calculation results because the XPS results in Section 3.2 confirm that N defects could be introduced into all different N sites.

Furthermore, some new states (defect states) appear between the CBM and VBM of N-defective g-C_3N_4, which is ascribed to the carbon dangling bond due to the generation of nitrogen vacancies.[57] The defect state mechanism has been recently applied to explain the improved light absorption capability of photocatalysts such as TiO_2[58] and ZnO[59] with oxygen vacancies and g-C_3N_4 with carbon and nitrogen vacancies.[25,26] In **Figure** 6a,b), the favorable effects of introducing defect states into photocatalysts can be summarized into the following aspects: 1) acting as an interband to accommodate photoelectrons excited by photons with energy lower than the bandgap to enhance the light absorbance capacity; 2) enabling the electrons to transit from defect states to CBM to further promote the electron transition from VB to CB and promoting the separation efficiency of photogenerated electron-hole pairs.[11,17] Notably, the position of defect state can be tuned by altering the position and density of generated nitrogen defects. Figure 6c demonstrates that the energy bandgap between the defect state and VBM with the generation of nitrogen defects in different N sites exhibits a sequential order of N2>N3>N1>N2N3>N1N3>N1N2>N1N2N3, indicating that the defect states may shift closer to the edge of the VB with increasing density of generated N defects in g-C_3N_4. Additionally, the positions of defect states in pristine UCN, etched UCN-0.5 h, etched UCN-1 h, and etched UCN-2 h were approximately estimated by the Urbach tail in Figure 3e, and the results show that the estimated defect states shifted closer to the VB with prolonged $NaBH_4$ treatment time, coinciding with the calculation results that a higher N defect density can induce a deeper downshifting of the defect state to the VB. In addition, etched UCN-1 h exhibited the best photocatalytic activity, indicating that the defect states may shift closer to the edge of the VB with increasing density of N vacancies, leading to the formation of deeper defect states to accommodate more charge carriers excited by photons at longer wavelengths. Nevertheless, with deeper downshifting to the VBM (Figure 6b), the structure of g-C_3N_4 may be destroyed if there are excessive nitrogen defects generated and the defect states could become a new center for the recombination of electrons and holes,[11] leading to the deterioration of photocatalytic activity, which can explain the obviously decreased photocatalytic CIP degradation performance of etched UCN-2 h compared to that of etched UCN-1 h.

Partial density of states (PDOS) analysis was further employed to describe the contribution of different atoms to the modification of band structures in g-C_3N_4. Figure 5a suggests that the CBM of the perfect structure and defective structures with different N vacancies mainly consisted of C-2p and N-2p orbitals, while the VBM is predominantly composed of N-2p orbitals, which is consistent with previous reports.[18,26,57] Notably, these C-2p and N-2p states are changed both in the conduction and valence bands with the incorporation of N defects at different sites. Furthermore, the newly formed defect states in different defective structures are primarily contributed by N-2p and C-2p orbitals, which is also in accordance with other reports.[26,57,60] The analysis (Figure S9, Supporting Information) of the projected contribution of C and N orbitals to the band energies further illustrates the evolution of the band structure of UCN by introducing nitrogen defects into different nitrogen sites. Hence, the theoretical calculation results elucidate that the generation of N defects in heptazine-based g-C_3N_4 could lead to the reconstruction of the band structure.

Figure 7 displays the highest occupied molecular orbital (HOMO) and lowest unoccupied molecular orbital (LUMO) locations in perfect g-C_3N_4 and N-defective g-C_3N_4. It is clear that the HOMO and LUMO are uniformly delocalized over the heptazine unit in the structure of perfect g-C_3N_4 because of the high symmetry of its framework.[26] Notably, no HOMO localized on bridge N1 in the perfect structure, indicating that no electrons could be excited from N1 atoms under light illumination.[56] This observation further explains the weak photocatalytic activity of pristine UCN for CIP degradation in this work. Comparatively, apparent redistribution of the charge density and spatial separation of the HOMO and LUMO are observed in all the structures with N defects, leading to the generation of electron-rich regions in or around the positions of the N defects. Such localized charge accumulation could contribute to the shifting of the VB and CB,[26,55] and the introduction of defect states between the VB and CB was observed in the above band structure and PDOS results. Importantly, the spatial separation of the HOMO and LUMO is beneficial inhibiting the recombination of charge carriers, thus promoting their separation efficiency and increasing the chance of interfacial charge transfer for the generation of reactive species.[55,56] These observations provide fundamental information to explain the significant improvement in the photocatalytic performance of etched UCN in this work. In addition, a certain overlap of the HOMO and LUMO could be observed around the N1 site in the structure with N2N3 defects, which could contribute to the calculated higher bandgap, as discussed above.

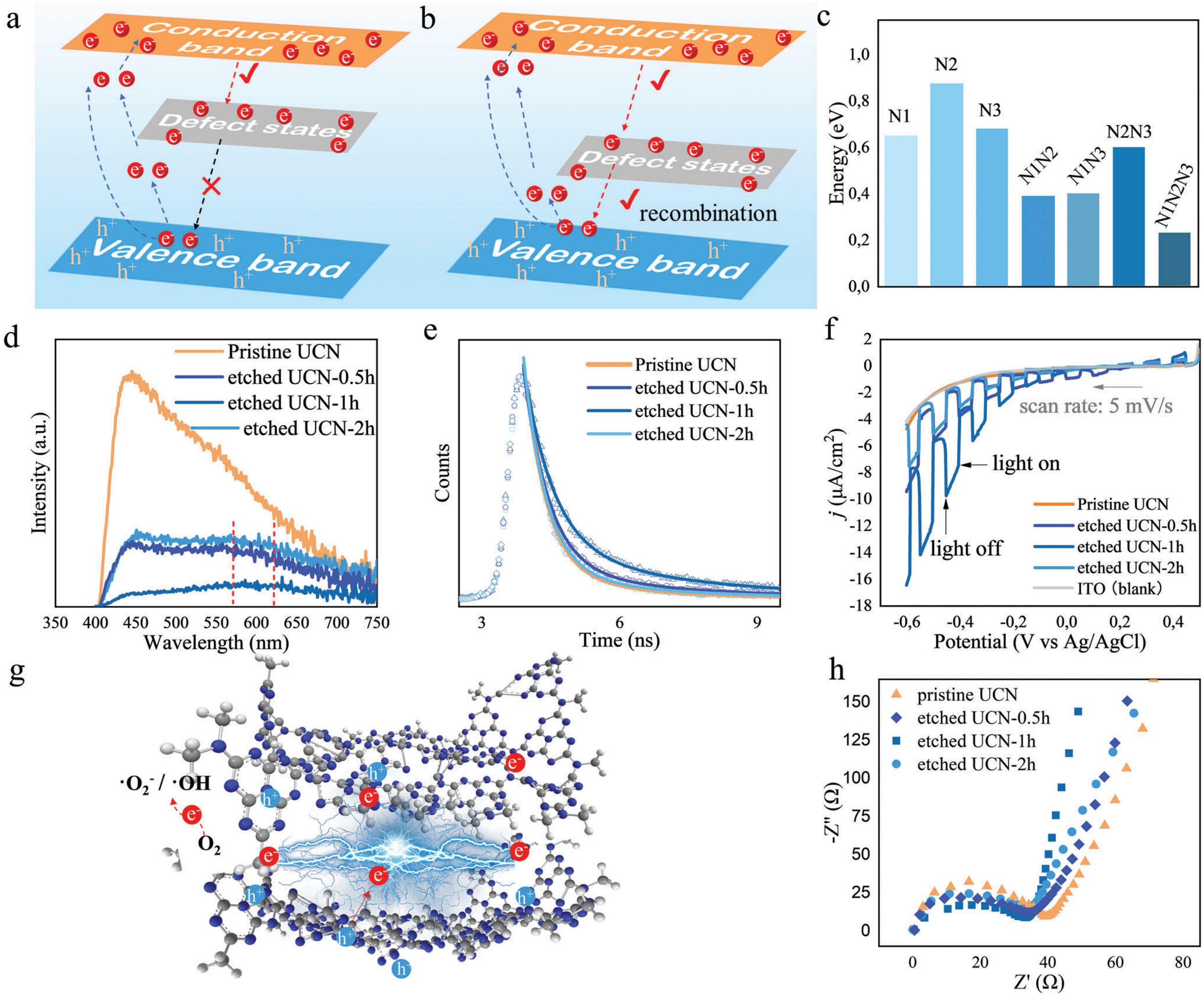

Figure 6. Illustration of the a) separation and b) recombination of photoexcited electrons and holes in etched UCN with defect states downshifting to the VBM, DFT calculated energy gap between defect states and VBM in g-C_3N_4 with different N defect densities c), steady-state PL emission spectra (excitation at 375 nm) d), time-resolved PL decay spectra by time-correlated single-photon counting e), transient photocurrent response f), interfacial charge property diagram of etched UCN-1 h g) and h) EIS curves of different UCN samples.

2.5.2. Improved Charge Carrier Separation and Transportation

As discussed in the theoretical calculation section, the introduced defect states could act as an interband to accommodate excited electrons to enhance the separation efficiency of photogenerated electron-hole pairs and may also downshift to a critical position with the increase in the generated N defect density, which is close enough to the VBM to become a new recombination center for photogenerated electron-hole pairs. The steady-state photoluminescence (PL) emission spectra were recorded to explore the impact of N defects on the charge transfer dynamics of the prepared samples. In Figure 6d, an obvious PL emission peak attributed to the radiative recombination of charge carrier centers at ≈450 nm was observed in all samples,[61] which was gradually quenched for etched UCN with $NaBH_4$ treatment time from 0 to 1 h, while the intensity of the peak in etched UCN-2 h was strengthened compared to that in etched UCN-1 h. Furthermore, a few new emission peaks appeared in the range of 500–700 nm in etched UCN samples, which could correspond to the vibrational relaxation of excited state electrons to the new states, implying the successful introduction of defect states between VB and CB.[61] Moreover, the intensity changes and redshift of these new peaks were also observed in etched UCN samples, where etched UCN-1 h exhibited a more significant peak intensity change and shifting than etched UCN-0.5 h and etched UCN-2 h, further indicating that the position of introduced defect states could be shifted with the change in introduced N defect density in etched UCN and that the defect states could also become new recombination centers for photogenerated electron-hole pairs. Such observed PL quenching implies that the intrinsic radiative recombination of the photogenerated electron-hole pairs could be inhibited by the suitable introduction

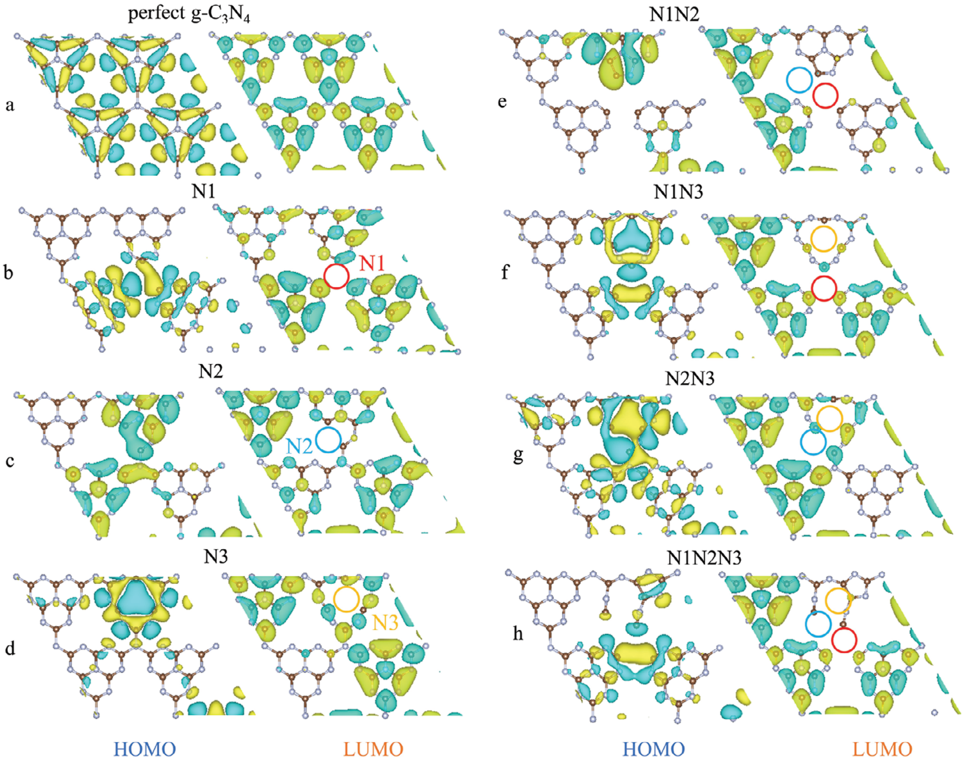

Figure 7. HOMO and LUMO distribution of perfect a) and N-defective g-C_3N_4 structures with b) N1, c) N2, d) N3, e) N1N2, f) N1N3, g) N2N3, and h) N1N2N3 defect sites.

of N defects in UCN,[26,35] which is consistent with the DFT results.

Time-correlated single-photon counting (TCSPC) spectra were further recorded to examine the lifetimes of the charge carriers in the UCN samples, as shown in Figure 6e. All spectra decay exponentially, where the etched UCN-1 h exhibited the lowest fluorescent decay kinetics. As mentioned above, a longer fluorescence lifetime normally suggests a better separation of photogenerated electron-hole pairs, where τ_1 and τ_2 are assigned to the fast recombination of excitons, while the relatively long-lasting lifetime τ_3 relates to most of the detected photons.[62,63] The fluorescence lifetimes of the UCN samples are listed in Table S5 (Supporting Information), where the pristine UCN, etched UCN-0.5 h, etched UCN-1 h, and etched UCN-2 h exhibit an average fluorescence lifetimes of 1.739, 3.099, 3.9789, and 2.072 ns, respectively. This result is consistent with the photocatalytic degradation of CIP by the different UCN samples described in Section 2.4. Notably, the values of both τ_1 and τ_2 of the UCN samples first increase with increasing $NaBH_4$ treatment time from 0 to 1 h but decrease with further increase to 2 h (Table S5, Supporting Information). Interestingly, the percentage of τ_1 exhibited a reverse trend in contrast to that of τ_2, where τ_1 decreased with increasing $NaBH_4$ treatment time from 0 to 1 h but further increased from 1 to 2 h. Combining the change trends of these fluorescence lifetime values and their corresponding percentages with the above experimental and DFT calculation results, τ_1 and τ_2 could be mainly interpreted as the recombination of electrons in the CBM with holes in the VBM and the recombination of electrons in defect states with holes in the VBM, respectively.[62–64] The experimental and DFT calculation results confirmed that the suitable introduction of N defects in etched UCN is favorable for promoting the separation efficiency of electron-hole pairs by narrowing the bandgap and introducing a defect state as an interband to accommodate electrons. The bandgap of etched UCN gradually narrows with increasing $NaBH_4$ treatment time from 0 to 1 h, leading to an increase in the separation efficiency of electron-hole pairs and corresponding τ_1 values. Moreover, the defect states could be downshifted with increasing defect density in etched UCN to accommodate more electrons excited by lower energy. These electrons excited by lower energy could only localize in the defect state or recombine with electrons in the VBM because they cannot overcome the energy gap to further jump to the CBM, leading to a decrease in the percentage of τ_1 and an increase in the τ_2 values and their corresponding percentages in the UCN samples. Moreover, the changes in the τ_1 and τ_2 values and their relevant percentages in etched UCN-2 h might be explained by the quantum effect induced by the deteriorated structure and reduced size and the fact that defect states with a greater N defect density could become new recombination centers for charge carriers. In addition, the percentage of τ_3 for the UCN samples increases with increasing $NaBH_4$ treatment time from 0 to 1 h but decreases from 1 to 2 h, further elucidating the roles and downshifting of the incorporated defect state with increasing N defect density.

The transient photocurrent response was tested to further elucidate the impact of N defects on the separation and transportation of photogenerated electron-hole pairs. Figure 6f shows that the pristine UCN displays a neglectable photocurrent response under the illumination of simulated solar light as that of the

ITO blank, while etched UCN samples exhibit a significant improvement in the photocurrent response. Notably, etched UCN-1 h displays the highest photocurrent density value compared to other etched UCN samples, suggesting that etched UCN-1 h has the best separation and transport efficiency of photogenerated electron-hole pairs.[18,25] Additionally, the observed current density changes by switching on/off light collected from cyclic voltammetry in Figure S10 (Supporting Information) further confirm the generated photocurrent in etched UCN samples, where the cathode current density instantly increased with light illumination while immediately returning to the initial status by switching off the light. The etched UCN-1 h exhibited the strongest enhanced current density with light illumination, indicating that it has a higher photogenerated electron-hole pair separation efficiency to facilitate the generation of reactive species (Figure 6g). In addition, the EIS spectra in Figure 6h show that the arc radius of the samples decreases in the following order: pristine UCN > etched UCN-2 h > etched UCN-0.5 h > etched UCN-1 h. The results indicate that etched UCN-1 h demonstrated the lowest interfacial electron transfer resistance, further confirming that suitable N vacancies could be beneficial for promoting the separation of photogenerated charge carriers. The observed significant changes in the PL peak intensity, radiative lifetime, photocurrent density, and of the samples with different $NaBH_4$ treatment times demonstrate that the photocatalytic activity of UCN could be improved by introducing a suitable N defect density but further reduced in the case of overgenerated N defects, which is consistent with the calculation results of the shifting of defect states.

3. Conclusion

In summary, we have explored the impact of nitrogen defects on the photocatalytic activities of UCN for the degradation of CIP under simulated sunlight. Experiments and DFT calculations highlight that the introduced nitrogen defects could tune the band structure of UCN by incorporating defect states. The density of introduced nitrogen defects in UCN within optimum ranges exhibits a positive correlation with its photocatalytic activity owing to the gradually improved light absorption ability, charge carrier separation, and transfer efficiency. However, over-introduced nitrogen defects could lead to the over-downshifting of the defect state to the VBM, which could become a new recombination center for charge carriers. In addition, the quantum size effect may also affect the bandgap of etched UCN. This work provides deep insight into the construction of efficient nitrogen-defective UCNs for the capture and utilization of solar energy for CIP photocatalytic degradation.

4. Experimental Section

Chemicals: Ciprofloxacin (CIP, ≥98%), carbamazepine (CBZ, ≥98%), HPLC grade methanol (≥99.5%), and urea (99.5%) were purchased from Sigma–Aldrich (Germany). Sulfamethoxazole (SMX, 98%) was purchased from TCI Europe (USA). Sodium hydroxide (NaOH), hydrochloric acid (HCl), 1,4-benzoquinone (BQ, 99%), and sodium borohydride (99%) were provided by Acros Organics (Geel, Belgium). HPLC grade acetonitrile (CAN, ≥99.5%) and formic acid (FA, ≥98%) were provided by Fisher Chemical (UK) and Acros Organics (Belgium), respectively. All solutions were prepared using Milli-Q ultra-pure water (Millipore, USA). Compressed N_2 gas was supplied by Air Liquide (Liege, Belgium).

Synthesis of Pristine UCN and Etched UCN: Pristine UCN was fabricated by the direct calcination of urea in a muffle furnace at 550 °C for 2 h with a ramping rate of 10 °C min^{-1}. The obtained samples were ground into fine powder after cooling to room temperature for further application. The etched UCN was synthesized via $NaBH_4$ treatment. Briefly, 0.4 g UCN and 0.3 g $NaBH_4$ were mixed and ground uniformly, and then the mixture was dissolved in 15 mL Milli-Q water and heated to 60 °C for 1 h. The obtained slurry mixture sample was centrifuged to remove most water and subsequently calcinated at 300 °C for 15 min under a N_2 atmosphere. Finally, the obtained etched UCN sample was washed with water and ethanol to be neutral to remove impurities and dried for further use.

Performance Evaluation of Etched UCN for CIP Degradation: Typically, batch experiments were performed in a 250 mL black jacketed beaker. A G2V pico LED Solar Simulator (G2V Optics Inc., Canada) with irradiance equal to sun-equivalent (75.9 mW cm^{-2} base spectrum) was applied as simulated solar light. The emission spectrum of the light source is recorded in Figure S11 (Supporting Information). Unless specifically illustrated, the standard photocatalytic degradation experiments were carried out by illuminating 100 mL aqueous suspension containing 2.5 mg L^{-1} CIP and 0.5 g L^{-1} UCN. The temperature was 25 ± 1 °C, and the suspension was magnetically stirred at 500 rpm to keep it well mixed. The initial pH of the CIP solution was ≈6.0, which was not buffered in any experiment. At given time intervals, aliquots of the suspension were sampled and filtered through a 0.45 μm membrane filter, and 0.20 mL of methanol was added to a 0.80 mL sample to prevent further CIP degradation by residual reactive species. Then, the concentration of CIP, CBZ, and SMX was determined by high-performance liquid chromatography (HPLC) and the description of the analytic method is given in Text S1 (Supporting Information). The impact of common organic components (humic acid, HA) and inorganic substances (i.e., chloride, nitrate, sulfate, and bicarbonate) in wastewater on CIP photocatalytic degradation was investigated. In addition, a cyclic experiment was performed to study the reusability and stability of etched UCN. To this end, the etched UCN used was first collected by centrifugation and then directly dried at 60 °C for the next cycle.

Photoelectrochemical Measurement: Photoelectrochemical experiments of all samples were conducted in a three-electrode system by utilizing an AUOT Lab workstation. The samples coated with indium-tin oxide (ITO) glass, a Pt wire, a Ag/AgCl (saturated KCl) electrode, and 0.5 M Na_2SO_4 were applied as the working electrode, counter electrode, reference electrode, and electrolyte, respectively. The preparation process of the working electrodes was as follows. Twenty milligrams of UCN sample and 50 μL of Nafion solution (5 wt.%) were dispersed into 450 μL of isopropanol to prepare homogeneous catalyst ink by ultrasonication for 30 min. Next, 40 μL of catalyst ink was deposited onto ITO with an area of 1 cm^2 and then dried at room temperature for 1 h for further use. The photocurrent response was recorded by chopped liner sweep voltammetry at a voltage range from 0.5 to −0.6 V versus Ag/AgCl with a scan rate of −5 mV s^{-1} by using a G2V pico LED Solar Simulator. Cyclic voltammetry curves were obtained in the voltage range from 0.5 to −0.6 V versus Ag/AgCl with a scan rate of 30 mV s^{-1} to study the current density changes with and without light irradiation. Electrochemical impedance spectroscopy (EIS) was recorded under open circuit voltage over a frequency range from 10^5 to 0.1 Hz.

Characterization: XRD (Panalytical X'Pert PRO, Netherlands) was performed to study the composition and crystallinity of the samples. FTIR spectroscopy was carried out on a Bruker Alpha II instrument with an attenuated total reflection diamond accessory. BET analysis was performed to obtain N_2 absorption-desorption isotherms by using a Micromeritics Gemini V2. EPR experiments were conducted on a Bruker A300 with $f = 9.7688$ GHz at room temperature. PL emission spectra and time-resolved transient PL decay spectra were obtained at room temperature by applying an Edinburgh FLS1000 fluorescence spectrophotometer, which employed a xenon lamp with an excitation wavelength of 375 nm. Time-resolved fluorescence decay spectra were recorded by time-correlated single-photon counting (TCSPC), which were calculated by Equation (6):[63]

$$I\,(t) = A_1 \exp\left(-t/\tau_1\right) + A_2 \exp\left(-t/\tau_2\right) + A_3 \exp\left(-t_0/\tau_3\right) / \left(1 - \exp\left(-t/\tau_3\right)\right) \tag{6}$$

where A_i and τ_i (i = 1, 2, 3) are the amplitudes and lifetimes of luminescent components, respectively. The fluorescence lifetime represents the radiative recombination of photogenerated charge carriers and accounts for most of the detected photons.

Solid-state ^{13}C cross-polarization magic angle spinning NMR spectra were obtained on a Bruker AVANCE III 400 MHz WB solid-state NMR spectrometer at room temperature. XPS was performed on a Thermo Scientific K-Alpha with a monochromatized A1 Kα line source (1486.6 eV), and the binding energy was calibrated using the C1s peak at 284.8 eV. UV–vis DRS spectra were obtained on a UV-2600 spectrophotometer (Shimadazu) at room temperature. SEM and TEM images were obtained by Hitachi SU-70 and STEM HD2700 (Hitachi, Japan).

Computational Methods: All calculations were performed in the framework of density functional theory with the projector augmented plane-wave method, as implemented in the Vienna ab initio simulation package.[65] The generalized gradient approximation (GGA) in the Perdew-Burke-Ernzerhof (PBE) scheme was applied for the exchange-correlation potential calculation.[66] The cut-off energy for the plane wave was set to 520 eV. Brillouin zone integration was performed at the Gamma point with a 6 × 6 × 1 k-mesh grid. The energy criterion was set to 10^{-6} eV in an iterative solution of the Kohn-Sham equation. All the structures were relaxed until the residual forces on the atoms decreased to less than 0.02 eV Å^{-1}. The 2 × 2 (56 atoms) supercell, reported to be sufficient to represent g-C_3N_4 sheets by other researchers, was applied as the basis for the calculation of different N defeats in-heptazine-based g-C_3N_4.[57,60] A vacuum spacing of 20 A° along the z axis was applied to avoid spurious interactions caused by the periodic image. It is noted that the GGA-PBE function may underestimate the bandgap of g-C_3N_4 due to the well-known limitations of DFT. However, the GGA-PBE function was successfully applied by many researchers to interpret the impact of element doping and defects on the electronic structures and improved photocatalytic activity of different photocatalysts.[25,51,52] Moreover, it might be computationally expensive to calculate the 2 × 2 supercell by using a relatively accurate hybrid function. Most importantly, this study mainly aimed to qualitatively instead of quantitively investigate the impact of N vacancies incorporated at different N sites on the electronic structure of g-C_3N_4. Hence, the GGA-PBE function was selected and expected to be sufficient to achieve this goal.

The nitrogen defect formation energy (E_f) was calculated by Equation (7):[67]

$$E_f = E_{\text{defective}} - E_{\text{perfect}} + \mu\,(\text{N}) \tag{7}$$

where $E_{\text{defective}}$, E_{perfect} and μ (N) represent the total energy of N-defective, perfect g-C_3N_4 and the chemical potentials of the N atom, respectively.

Supporting Information

Supporting Information is available from the Wiley Online Library or from the author.

Conflict of Interest

The authors declare no conflict of interest.

Data Availability Statement

The data that support the findings of this study are available from the corresponding author upon reasonable request.

Keywords

defect state, g-C_3N_4, nitrogen defect, quantum size effect

Received: April 3, 2024
Revised: June 6, 2024

---

[1] H. Wang, H. Wang, Z. Wang, L. Tang, G. Zeng, P. Xu, M. Chen, T. Xiong, C. Zhou, X. Li, D. Huang, Y. Zhu, Z. Wang, J. Tang, *Chem. Soc. Rev.* **2020**, *49*, 4135.
[2] S. Cong, J. Cai, X. Li, J. You, L. Wang, X. Wang, *Adv. Funct. Mater.* **2024**, 2401540.
[3] R. Su, Y. Zhu, B. Gao, Q. Li, *Water Res.* **2024**, *251*, 121119.
[4] S. Bai, J. Jiang, Q. Zhang, Y. Xiong, *Chem. Soc. Rev.* **2015**, *44*, 2893.
[5] W. Li, A. Elzatahry, D. Aldhayan, D. Zhao, *Chem. Soc. Rev.* **2018**, *47*, 8203.
[6] K. M. Lee, C. W. Lai, K. S. Ngai, J. C. Juan, *Water Res.* **2016**, *88*, 428.
[7] Q. Li, X. Li, S. Wageh, A. A. Al-Ghamdi, J. Yu, *Adv. Energy Mater.* **2015**, *5*, 1500010.
[8] A. Yang, J. Luo, Z. Xie, Q. Chen, *Appl. Surf. Sci.* **2022**, *599*, 153894.
[9] A. Sinhamahapatra, J. P. Jeon, J. Kang, B. Han, J. S. Yu, *Sci. Rep.* **2016**, *6*, 27218.
[10] Y. Zheng, L. Lin, B. Wang, X. Wang, *Angew. Chem., Int. Ed.* **2015**, *54*, 12868.
[11] S. Bai, N. Zhang, C. Gao, Y. Xiong, *Nano Energy* **2018**, *53*, 296.
[12] X. Duan, H. Jia, T. Cao, H. Yu, Y. Zhang, Y. Lu, D. Zhou, *Appl. Catal., B.* **2024**, *352*, 124016.
[13] Y. Yang, Y. Guo, F. Liu, X. Yuan, Y. Guo, S. Zhang, W. Guo, M. Huo, *Appl. Catal. B.* **2013**, *142*, 828.
[14] Y. Zheng, L. Lin, B. Wang, X. Wang, *Angew. Chem., Int. Ed.* **2015**, *54*, 12868.
[15] Q. Han, B. Wang, J. Gao, Z. Cheng, Y. Zhao, Z. Zhang, L. Qu, *ACS Nano.* **2016**, *10*, 2745.
[16] X. Yang, Y. Ye, J. Sun, Z. Li, J. Ping, X. Sun, *Small* **2022**, *18*, 2105089.
[17] X. Xu, Y. Xu, Y. Liang, H. Long, D. Chen, H. Hu, J. Z. Ou, *Mater. Chem. Front.* **2022**, *6*, 3143.
[18] T. Yu, T. Xie, W. Zhou, Y. Zhang, Y. Chen, B. Shao, W. Q. Guo, X. Tan, *ACS Sustainable Chem. Eng.* **2021**, *9*, 7529.
[19] X. Chen, J. Zhang, X. Fu, M. Antonietti, X. Wang, *J. Am. Chem. Soc.* **2009**, *131*, 11658.
[20] X. Wang, X. Chen, A. Thomas, X. Fu, M. Antonietti, *Adv. Mater.* **2009**, *21*, 1609.
[21] Y. Wang, W. Yang, X. Chen, J. Wang, Y. Zhu, *Appl. Catal. B.* **2018**, *220*, 337.
[22] J. Zhang, M. Zhang, R.-Q. Sun, X. Wang, J. Zhang, M. Zhang, R. Sun, X. Wang, *Angew. Chem., Int. Ed.* **2012**, *51*, 10145.
[23] C. Shubin Yang, Y. Gong, J. Zhang, L. Zhan, L. Ma, Z. Fang, R. Vajtai, X. Wang, P. M. Ajayan, S. B. Yang, L. Zhan, L. L. Ma, R. Vajtai, P. M. Ajayan, Y. J. Gong, X. C. Wang, J. S. Zhang, Z. Y. Fang, *Adv. Mater.* **2013**, *25*, 3840.
[24] N. Tian, K. Xiao, Y. Zhang, X. Lu, L. Ye, P. Gao, T. Ma, H. Huang, *Appl. Catal. B.* **2019**, *253*, 196.
[25] W. Tu, Y. Xu, J. Wang, B. Zhang, T. Zhou, S. Yin, S. Wu, C. Li, Y. Huang, Y. Zhou, Z. Zou, J. Robertson, M. Kraft, R. Xu, *ACS Sustainable Chem. Eng.* **2017**, *5*, 7260.
[26] D. Zhao, C.-L. Dong, B. Wang, C. Chen, Y.-C. Huang, Z. Diao, S. Li, L. Guo, S. Shen, D. Zhao, B. Wang, Z. Diao, L. Guo, S. Shen, C. Dong, Y. Huang, C. Chen, S. Li, *Adv. Mater.* **2019**, *31*, 1903545.
[27] Y. Li, M. Gu, M. Zhang, X. Zhang, K. Lv, Y. Liu, W. Ho, F. Dong, *Chem. Eng. J.* **2020**, *389*, 124421.

[28] J. Wu, N. Li, H. Bin Fang, X. Li, Y. Z. Zheng, X. Tao, *Chem. Eng. J.* **2019**, *358*, 20.

[29] Y. Wen, D. Qu, L. An, X. Gao, W. Jiang, D. Wu, D. Yang, Z. Sun, *ACS Sustainable Chem. Eng.* **2019**, *7*, 2343.

[30] Y. Qin, J. Lu, X. Y. Zhao, X. Lin, Y. Hao, P. Huo, M. Meng, Y. Yan, *Chem. Eng. J.* **2021**, *425*, 131844.

[31] G. Zhang, M. Zhang, X. Ye, X. Qiu, S. Lin, X. Wang, G. Zhang, M. Zhang, X. Ye, X. Qiu, S. Lin, X. Wang, *Adv. Mater.* **2014**, *26*, 805.

[32] G. Zhang, C. Huang, X. Wang, *Small* **2015**, *11*, 1215.

[33] V. W. H. Lau, I. Moudrakovski, T. Botari, S. Weinberger, M. B. Mesch, V. Duppel, J. Senker, V. Blum, B. V. Lotsch, *Nat. Commun.* **2016**, *7*, 12165.

[34] T. Jiang, Z. Wang, G. Wei, S. Wu, L. Huang, D. Li, X. Ruan, Y. Liu, C. Jiang, F. Ren, *ACS Energy Lett.* **2024**, *9*, 1915.

[35] D. Zhao, Y. Wang, C. L. Dong, Y. C. Huang, J. Chen, F. Xue, S. Shen, L. Guo, *Nat. Energy* **2021**, *6*, 388.

[36] Y. Jiang, Z. Sun, C. Tang, Y. Zhou, L. Zeng, L. Huang, *Appl. Catal., B.* **2019**, *240*, 30.

[37] Z. Zhu, H. Pan, M. Murugananthan, J. Gong, Y. Zhang, *Appl. Catal., B.* **2018**, *232*, 19.

[38] H. Fattahimoghaddam, T. Mahvelati-Shamsabadi, B. K. Lee, *ACS Sustainable Chem. Eng.* **2021**, *9*, 4520.

[39] C. Kaiser, O. J. Sandberg, N. Zarrabi, W. Li, P. Meredith, A. Armin, *Nat. Commun.* **2021**, *12*, 3988.

[40] N. Khatun, E. G. Rini, P. Shirage, P. Rajput, S. N. Jha, S. Sen, *Mater Sci. Semicond. Process.* **2016**, *50*, 7.

[41] M. Singh, M. Goyal, K. Devlal, *J. Taibah Univ. Sci.* **2018**, *12*, 470.

[42] Y. Wu, L. Bu, X. Duan, S. Zhu, M. Kong, N. Zhu, S. Zhou, *J. Cleaner Prod.* **2020**, *273*, 123065.

[43] D. T. Oyekunle, J. Cai, E. A. Gendy, Z. Chen, *Chemosphere* **2021**, *280*, 130949.

[44] A. Asghar, H. V. Lutze, J. Tuerk, T. C. Schmidt, *J. Hazard. Mater.* **2022**, *429*, 128189.

[45] W. A. Arnold, *Environ. Sci.: Processes Impacts* **2014**, *16*, 832.

[46] J. Deng, Y. Ge, C. Tan, H. Wang, Q. Li, S. Zhou, K. Zhang, *Chem. Eng. J.* **2017**, *330*, 1390.

[47] Y. Liu, M. Kamali, X. Chen, B. Rossi, L. Appels, R. Dewil, *Chem. Eng. J.* **2024**, *493*, 151950.

[48] H. F. Miao, M. Cao, D. Y. Xu, H. Y. Ren, M. X. Zhao, Z. X. Huang, W. Q. Ruan, *Chemosphere* **2015**, *119*, 326.

[49] Z. Jia, T. Li, Z. Zheng, J. Zhang, J. Liu, R. Li, Y. Wang, X. Zhang, Y. Wang, C. Fan, *Chem. Eng. J.* **2020**, *380*, 122422.

[50] S. Li, T. Huang, P. Du, W. Liu, J. Hu, *Water Res.* **2020**, *185*, 116286.

[51] T. Li, N. Tsubaki, Z. Jin, *J. Mater. Sci. Technol.* **2024**, *169*, 82.

[52] W. J. Jo, J. W. Jang, K. J. Kong, H. J. Kang, J. Y. Kim, H. Jun, K. P. S. Parmar, J. S. Lee, *Angew. Chem., Int. Ed.* **2012**, *51*, 3147.

[53] X. Ma, Y. Lv, J. Xu, Y. Liu, R. Zhang, Y. Zhu, *J. Phys. Chem. C.* **2012**, *116*, 23485.

[54] Z. F. Huang, J. Song, L. Pan, Z. Wang, X. Zhang, J. J. Zou, W. Mi, X. Zhang, L. Wang, *Nano Energy* **2015**, *12*, 646.

[55] S. Hou, X. Gao, X. Lv, Y. Zhao, X. Yin, Y. Liu, J. Fang, X. Yu, X. Ma, T. Ma, D. Su, *Nano-Micro Lett.* **2024**, *16*, 1.

[56] Y. Wang, Y. Tian, L. Yan, Z. Su, *J. Phys. Chem. C* **2018**, *122*, 7712.

[57] S. P. Sun, Y. R. Wang, S. Gu, B. Wang, J. H. Sun, Y. Jiang, *Vacuum* **2022**, *206*, 111483.

[58] S. K. Cushing, F. Meng, J. Zhang, B. Ding, C. K. Chen, C. J. Chen, R. S. Liu, A. D. Bristow, J. Bright, P. Zheng, N. Wu, *ACS Catal.* **2017**, *7*, 1742.

[59] H. L. Guo, Q. Zhu, X. L. Wu, Y. F. Jiang, X. Xie, A. W. Xu, *Nanoscale* **2015**, *7*, 7216.

[60] X. Liu, W. Kang, W. Zeng, Y. Zhang, L. Qi, F. Ling, L. Fang, Q. Chen, M. Zhou, *Appl. Surf. Sci.* **2020**, *499*, 143994.

[61] Z. Qin, F. Xue, Y. Chen, S. Shen, L. Guo, *Appl. Catal. B.* **2017**, *217*, 551.

[62] P. Niu, G. Liu, H. M. Cheng, *J. Phys. Chem. C* **2012**, *116*, 11013.

[63] M. V. Dozzi, C. D'Andrea, B. Ohtani, G. Valentini, E. Selli, *J. Phys. Chem. C.* **2013**, *117*, 25586.

[64] C. Cheng, J. Zhang, B. Zhu, G. Liang, L. Zhang, J. Yu, *Angew. Chem., Int. Ed.* **2023**, *62*, 202218688.

[65] G. Kresse, D. Joubert, *Phys. Rev. B.* **1999**, *59*, 1758.

[66] J. P. Perdew, K. Burke, M. Ernzerhof, *Phys. Rev. Lett.* **1996**, *77*, 3865.

[67] C. Zhang, D. Qin, Y. Zhou, F. Qin, H. Wang, W. Wang, Y. Yang, G. Zeng, *Appl. Catal., B.* **2022**, *303*, 120904.